Rapid Communications

Coulomb excitations in ABC-stacked trilayer graphene

Chiun-Yan Lin,[1] Ming-Hsun Lee,[1] and Ming-Fa Lin[1,2,3,*]
[1]*Department of Physics, National Cheng Kung University, Tainan, Taiwan*
[2]*Hierarchical Green-Energy Materials Research Center, National Cheng Kung University, Tainan, Taiwan*
[3]*Quantum Topology Center, National Cheng Kung University, Tainan, Taiwan*

(Received 2 March 2018; revised manuscript received 5 June 2018; published 30 July 2018)

The layer-based random-phase approximation is further developed to investigate electronic excitations in trilayer ABC-stacked graphene. All layer-dependent atomic interactions and Coulomb interactions are included in the dynamic charge screening. There exist rich and unique (momentum, frequency)-excitation phase diagrams, in which the complex single-particle excitations and five kinds of plasmon modes are dominated by unusual energy bands and doping carrier densities. The latter frequently experience significant Landau damping due to the former, leading to coexistence or destruction in the energy-loss spectra. Specifically, the dispersion of the only acoustic plasmon in the pristine case is dramatically changed from linear to square root, even at very low doping.

DOI: 10.1103/PhysRevB.98.041408

Few-layer graphenes are one of the mainstream two-dimensional (2D) materials since their discovery by mechanical exfoliation on Bernal graphite in 2004 [1]. Such systems have unique geometric structures, nanoscaled thicknesses, a honeycomb lattice with two sublattices, a layered structure, and distinct stacking configurations. They are very suitable for studying diverse physical phenomena, such as massless/massive fermions [2,3], Coulomb excitations/deexcitations [4–14], quantized Landau levels [15–17], magneto-optical selection rules [17,18], and quantum Hall effects [19]. Specifically, the electronic excitations arising from the electron-electron (e-e) interactions play critical roles in the energy and width of quasiparticle states. Graphene-related systems have great potential as next-generation plasmonics for terahertz to midinfrared applications because of their unique and tunable collective excitations [20–24]. This Rapid Communication is focused on the rich Coulomb excitation spectra of ABC-stacked trilayer graphene. The relationship between the momentum-frequency phase diagram and the Fermi energy is investigated in detail.

Up to now, the stacking configurations identified in synthesized graphene systems cover ABC [25–28], ABA [27], AAB [29], and AAA [30]. They are the critical factor in determining the essential low-energy properties, e.g., the $2p_z$-orbital-induced π-electronic structures. Among them, the ABC stacking, being predicted to have the lowest ground-state energy [31], is frequently observed in experimental syntheses. This system presents very rich band structures under the various vertical and nonvertical interlayer atomic interactions. For example, trilayer ABC stacking possesses three pairs of weakly dispersive, sombrero-shaped, and linear energy bands [Fig. 1(a)]. Such energy dispersions will be directly reflected in other physical properties, e.g., the optical spectra [17,28] and low-frequency plasmon modes.

Many theoretical [4–8] and experimental [9–14] studies on the Coulomb excitations of graphene-related systems have been conducted. The single-particle and collective excitations (SPEs and plasmons) are very sensitive to the stacking configurations, the number of layers, the electric and magnetic fields, and the dimensions. An intrinsic monolayer graphene only possesses interband single-particle excitations (SPEs) at zero temperature because of the zero-gap semiconductor [32]. Three plasmon modes are revealed in bilayer AA stacking, but not in bilayer AB stacking [6,7]. The fact that the former has a sufficiently high free-carrier density due to the interlayer atomic interactions accounts for this important difference. In extrinsic few-layer graphenes the doping-free carriers can create rich SPEs and plasmon modes [5–7]. However, most of the theoretical predictions only consider the electronic excitations arising from the first pair of valence and conduction bands nearest to the Fermi level (E_F). The fully dynamic charge screening due to all the pairs of energy bands are included in the current calculations, so that diverse Coulomb excitation spectra can be presented in momentum- and frequency-dependent phase diagrams.

For the ABC-stacked trilayer graphene, the band-structure and Coulomb interactions are, respectively, evaluated from the tight-binding model and random-phase approximation (RPA). Specifically, the intralayer and the interlayer atomic interactions and Coulomb interactions are fully taken into consideration; furthermore, layer-based polarization functions and dielectric functions are built from sublattice-dependent tight-binding functions. Many kinds of SPE channels and plasmon modes are explored in detail, especially for the strong dependence of electronic excitations on the magnitude of transferred momentum (q) and E_F. The predicted results could be verified by high-resolution electron-energy-loss spectroscopy (EELS) [11,12] and inelastic light scattering spectroscopy [13,14].

As shown in Fig. 1(a), the ABC-stacked trilayer graphene has significant interlayer atomic interactions (β_1–β_5) in addition to an intralayer one (β_0) [33]. The former creates

*mflin@mail.ncku.edu.tw

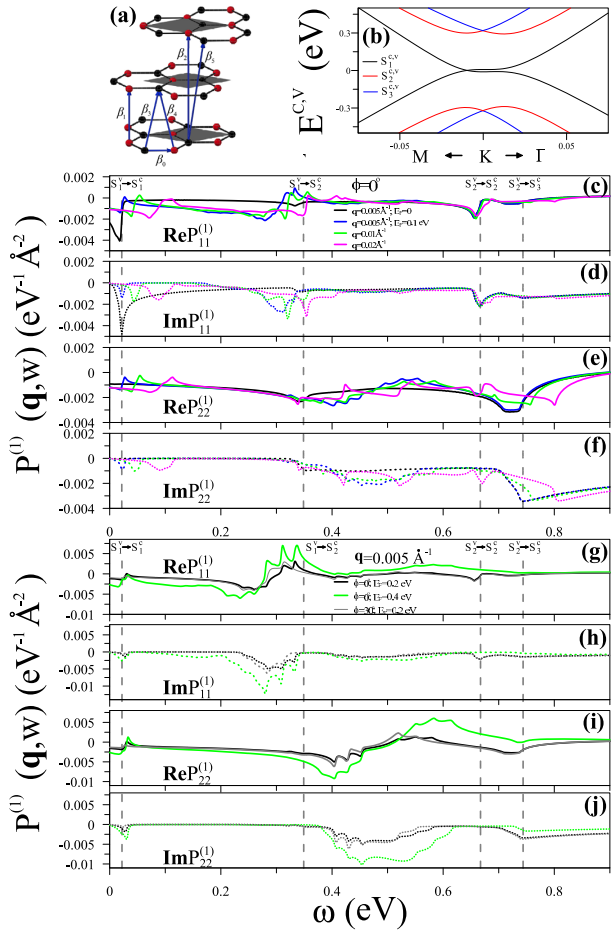

FIG. 1. (a) Geometric structure and (b) low-energy bands of ABC-stacked trilayer graphene. The Fermi level of the pristine graphene is set to be zero. (c) Imaginary and (d) real parts of $P_{11}^{(1)}$ at $E_F = 0$ and $E_F = 0.1$ eV for different q's. (e) and (f) correspond to those of $P_{22}^{(1)}$. (g)–(j) are related plots for $q = 0.01$ at various E_F's. ϕ is the angle between $\mathbf{q}$ and $\overrightarrow{\Gamma M}$.

the layer-dependent Coulomb excitation behavior. The π-electronic Hamiltonian is built from six $2p_z$-dependent tight-binding functions. There are three pairs of valence and conduction bands, corresponding to the weakly dispersive ($S_1^{c,v}$), sombrero-shaped ($S_2^{c,v}$), and linear ($S_3^{c,v}$) dispersions, as shown in Fig. 1(b). The first pair belongs to surface-localized states, since they mainly come from the top and bottom layers. The electronic structures of ABC-stacked trilayer graphenes have been verified by angle-resolved photoemission spectroscopy (ARPES) [34]. Specifically, the presence of surface-localized states has been clarified for the partially flat subbands centered at the K point. This will induce unusual electronic excitations, compared with other stacking systems. Each wave function is composed of six sublattice-based tight-binding functions, indicating the theoretical framework of the layer-dependent RPA.

When an electron beam is incident on the ABC-stacked trilayer graphene, the charge density distribution is assumed to be uniform inside each layer. The π electrons on distinct layers will screen the time-dependent external potentials [$V_{ll'}(\mathbf{q})$'s; the lth layer] via e-e interactions, leading to the induced charges and potentials. Within the linear response, the induced charge density is proportional to the effective Coulomb potentials [$V_{ll'}^{\text{eff}}(\mathbf{q}, \omega)$'s; ω is the transferred frequency during charge screening]. By using the layer-based RPA, the relationship among the effective, external, and induced Coulomb potentials is characterized by the Dyson equation [7],

$$\epsilon_0 V_{ll'}^{\text{eff}}(\mathbf{q}, \omega) = V_{ll'}(\mathbf{q}) + \sum_{m,m'} V_{lm}(\mathbf{q}) P_{m,m'}^{(1)}(\mathbf{q}, \omega) V_{m'l'}^{\text{eff}}(\mathbf{q}, \omega), \tag{1}$$

where ϵ_0 (=2.4) is the background dielectric constant. The external potential $V_{ll'}(\mathbf{q})$ is expressed as $v_q e^{-q|l-l'|I_c}$, where v_q ($= 2\pi e^2/q$) is the 2D bare Coulomb potential of a 2D electron gas, and the layer distance I_c is set as 3.35 Å^{-1} [31]. Apparently, the induced potential in the third term reveals the complicated dynamic screening due to the intralayer and interlayer Coulomb interactions. The layer-dependent bare polarization function, being determined by energy bands and wave functions, is expressed as

$$\begin{aligned} P_{mm'}^{(1)}(\mathbf{q}, \omega) = 2 \sum_{k} \sum_{n,n'} \sum_{h,h'=c,v} & \left(\sum_{i} u_{nmi}^{h}(\mathbf{k}) u_{n'm'i}^{h'*}(\mathbf{k}+\mathbf{q}) \right) \\ & \times \left(\sum_{i'} u_{nm'i'}^{h*}(\mathbf{k}) u_{n'm'i'}^{h'}(\mathbf{k}+\mathbf{q}) \right) \\ & \times \frac{f\left(E_n^h(\mathbf{k})\right) - f(E_{n'}^{h'}(\mathbf{k}+\mathbf{q}))}{E_n^h(\mathbf{k}) - E_{n'}^{h'}(\mathbf{k}+\mathbf{q}) + \hbar\omega + i\Gamma}. \end{aligned} \tag{2}$$

u_{nmi}^h is the amplitude of the wave function on the ith sublattice of the mth layer, arising from the valence/conduction state ($h = c$ and v) of the nth energy band. $f(E_n^h(\mathbf{k})) = 1/\{1 + \exp[(E_n^h(\mathbf{k}) - \mu(T))/k_B T]\}$ is the Fermi-Dirac distribution. k_B, $\mu(T)$, and Γ stand for the Boltzmann constant, chemical potential, and the energy width due to various deexcitation mechanisms, respectively. Moreover, the layer-dependent dielectric function is defined by the linear relationship between the effective and external potentials,

$$\epsilon_{ll'}(\mathbf{q}, \omega) = \epsilon_0 \delta_{ll'} - \sum_{m} V_{lm}(\mathbf{q}) P_{m,l'}^{(1)}(\mathbf{q}, \omega). \tag{3}$$

Using Eq. (3), one can express Eq. (1) as a linear tensor equation. The effective potential tensor is the inverse of the dielectric function tensor multiplied by the external potential tensor. The dimensional energy-loss function is useful in understanding the inelastic scattering probability of the EELS measurement [7,35],

$$\text{Im}[-1/\epsilon] \equiv \sum_{l} \text{Im}\left[- V_{ll}^{\text{eff}}(\mathbf{q}, \omega)\right] \Big/ \left(\sum_{l,l'} V_{ll'}(\mathbf{q})/3 \right). \tag{4}$$

Equations (1)–(4), which cover all the atomic and Coulomb interactions, are applicable to any layered graphene systems.

The dynamic Coulomb response displays SPEs and collective excitations as the transferred q and ω are conserved during e-e interactions. These two types of excitations are, respectively, characterized by the bare response function $P_{ll'}^{(1)}(\mathbf{q}, \omega)$ and energy-loss function $\text{Im}[-\frac{1}{\epsilon}]$. $P_{ll'}^{(1)}(\mathbf{q}, \omega)$ describes the dynamic charge screening and directly reflects the main features of the band structure. The imaginary part

$P^{(1)}_{ll'}(\mathbf{q},\omega)$ represents the strength of the SPEs and is responsible for the Landau damping. Im$[-\frac{1}{\epsilon}]$ is used to classify the plasmons in the screened Coulomb excitations. Collective excitations, or plasmons, appear at certain $(\mathbf{q},\omega)$ regions, where Im $P^{(1)}_{ll'}(\mathbf{q},\omega)$ is small, indicating the weak Landau damping. As shown in Figs. 1(c)–1(j), the interlayer polarizations ($l = l'$) and intralayer polarizations ($l \neq l'$) exhibit special structures associated with the critical points in the energy bands. In response to the dynamic Coulomb potential, Re$[P^{(1)}_{ll'}(\mathbf{q},\omega)]$ and Im$[P^{(1)}_{ll'}(\mathbf{q},\omega)]$ are linked to each other via the Kramers-Kronig relations [35]. The divergent singularities of Im$[P^{(1)}_{ll'}(\mathbf{q},\omega)]$ correspond to the van Hove singularities in the density of states (DOS). In ABC-stacked trilayer graphene, the 3×3 polarization function $P^{(1)}_{ll'}(\mathbf{q},\omega)$ depends on the symmetry of the wave function on each layer. Revealing the corresponding excitations, the intralayer and interlayer polarizations have similar structures, while their signs are determined by the phases of the wave functions. It is deduced that $P^{(1)}_{11} = P^{(1)}_{33}$, $P^{(1)}_{12} = P^{(1)}_{23}$, and $P^{(1)}_{11} \simeq |P^{(1)}_{13}|$ due to the geometric inversion symmetry in the ABC configuration. For $E_F = 0$ [black curves in Figs. 1(c)–1(f)], interband excitations give rise to divergent singularities of Im $P^{(1)}_{ll'}(\mathbf{q},\omega)$ (indicated by the dashed gray lines). The square-root peaks from the quasi-1D SPE channels, $S^v_1 \to S^c_1$ and $S^v_2 \to S^c_2$, appear as a result of the nearly isotropic energy dispersions near the K point [17]. Excitations from $S^v_1 \to S^c_2$ ($S^v_2 \to S^c_1$) and $S^v_2 \to S^c_3$ ($S^v_3 \to S^c_2$) exhibit a logarithmic form and display a relatively weak response. In particular, the surface-localized states play an important role for the low-energy polarizations. Near the Fermi level, the prominent square-root divergent structures of Im$[P^{(1)}_{11}(\mathbf{q},\omega)]$ arise from the major low-energy excitations on the outmost layers, while the empty Im$[P^{(1)}_{22}(\mathbf{q},\omega)]$ demonstrates the absence of excitations on the middle layer. Based on the Kramers-Kronig relations, the square-root and logarithmic peaks in Re$[P^{(1)}_{ll'}(\mathbf{q},\omega)]$ correspond to the square-root and step discontinuities in Im$[P^{(1)}_{ll'}(\mathbf{q},\omega)]$.

When E_F is higher, more electronic excitation channels are triggered with the increasing free carriers under the influence of the interlayer atomic interactions and Coulomb interactions. Consequently, this leads to complicated polarization functions. At $E_F = 0.1$ eV [Figs. 1(c)–1(f)], the interlayer and intralayer polarizations have a similar structure, in which the first logarithmic singularity of Im$[P^{(1)}_{ll'}(\mathbf{q},\omega)]$, shifting to higher ω with q, is mainly dominated by the SPEs within the $S^c_1 \to S^c_1$ intraband region. This channel determines the low-frequency excitation spectrum. On the other hand, the electronic states excited from the S^c_1 subband induce new SPEs reaching up to $\simeq 0.8$ eV (within the original interband region). It is claimed that when the energies of these SPEs coincide with those of plasmons, the plasmon intensity is weakened due to the Landau damping in the vicinity of the interband SPEs (dashed gray lines) [36]. When E_F is increased from 0.3 to 0.8 eV [Figs. 1(g)–1(j)], the polarization functions obviously display strong responses, and the intraband components gradually get more predominant than the interband ones. This implies that due to the interplay between interband and intraband excitations, the electronic excitation spectra can be diversified, and various plasmon modes are presented with a variation of q and E_F.

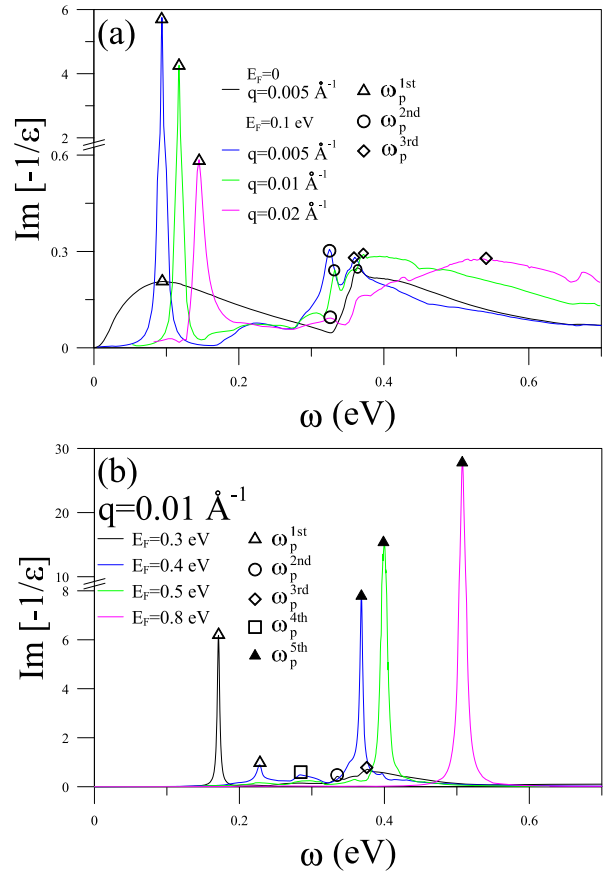

FIG. 2. Energy-loss spectra for (a) different q's, and (b) different E_F's.

The energy-loss function Im$[-\frac{1}{\epsilon}]$ is used to describe collective excitations, as shown in Fig. 2. Due to the screening effect, the plasmon frequency is in general higher than the corresponding SPE frequency. The peaks in Im$[-\frac{1}{\epsilon}]$ are referred to as plasmons. For $E_F = 0$ and $q = 0.005$ Å^{-1}, there are two intrinsic plasmon peaks, labeled by $\omega_p^{1\text{st}}$ and $\omega_p^{2\text{nd}}$, in the screened excitation spectrum of the pristine ABC-stacked trilayer graphene [black curve in Fig. 2(a)]. Identified from the specified interband channel, i.e., $S^v_1 \to S^c_1$, the plasmon energies correspond to the weak Landau damping given by the imaginary parts of the bare response function in Fig. 1. Responsible for the high DOS of the surface-localized states [26], the interband plasmon mode with ω up to 0.25 eV is classified as the first kind of plasmon, $\omega_p^{1\text{st}}$. In the energy region $\omega \simeq 0.32$ eV, the intensity decrease of Im$[-\frac{1}{\epsilon}]$ is attributed to the Landau damping that matches the energies of the $S^v_1 \to S^c_2$ SPEs. Modulated by the electron doping level, the loss function is enhanced for $E_F = 0.1$ eV by both intraband and interband excitations [blue curve in Fig. 2(a)]. There are three extrinsic plasmon modes, $\omega_p^{1\text{st}}$, $\omega_p^{2\text{nd}}$, and $\omega_p^{3\text{rd}}$. The first plasmon mode $\omega_p^{1\text{st}}$ ($\simeq$0.1 eV) is attributed to the $S^c_1 \to S^c_1$ intraband excitation channel, leading to a relatively prominent plasmon intensity. The latter two modes $\omega_p^{2\text{nd}}$ and $\omega_p^{3\text{rd}}$ near 0.3 eV mainly correspond to the $S^c_1 \to S^c_2$ and $S^v_1 \to S^c_1$ interband excitations, respectively; however, the higher excitations also make considerable contributions. With an increment of q, more available

SPE channels are triggered and the enhanced Landau damping quickly reduces the plasmons. The two plasmon modes decline and broaden as q increases from 0.005 to 0.02 Å^{-1}. On the other hand, the free-carrier excitations at a higher E_F lead to a dramatic change of the plasmon modes, as the doping level is higher than the critical point of the subbands S_2^c and S_3^c [Fig. 2(b)]. At $E_F = 0.4$ eV, the large suppression of the first peak implies the significant Landau dampings resulting from induced interband SPEs. On the other hand, there are two new types of plasmon modes, $\omega_p^{4\text{th}}$ and $\omega_p^{5\text{th}}$, which are ascribed to the multimode excitations of various intraband and interband channels. Under a sufficiently large E_F, e.g., $E_F = 0.5$, and 0.8 eV, there exists only one prominent peak, $\omega_p^{5\text{th}}$, of which the intensity and frequency are highly dependent on the densities of the free carriers. It should be noted that the dispersion of each plasmon mode is highly dependent on the boundaries of SPE channels and, moreover, for most interband excitations, plasmons and SPEs can coexist in a certain (q, ω) region.

Trilayer ABC-stacked graphene exhibits rich and unique plasmon spectra. Various plasmon modes are presented in the (q, ω)-excitation phase diagram (Figs. 3 and 4) under the influence of dynamic Coulomb interactions. In general, plasmons usually appear in specified domains of the (q, ω) diagram, because the Landau dampings occur in the region where the plasmon dispersion overlaps with the continuum spectrum of electron-hole pairs (solid and dashed curves) [36]. Near $E_F = 0$, there exists a strong SPE channel resulting from the excitations between S_1^v and S_1^c partially flat subbands. Under the screening effect, the corresponding collective excitations account for the low-ω plasmon branch. The dispersion relations of the intrinsic plasmons $\omega_p^{1\text{st}}$ and $\omega_p^{2\text{nd}}$ are shown in Fig. 3(a). The interband SPEs create strong Landau dampings near $\omega \sim 0.35$ and ~ 0.65 eV. In particular, the first plasmon $\omega_p^{1\text{st}}$ is assigned to an acoustic mode, of which the frequency approaches to zero as $\mathbf{q} \to \mathbf{0}$ [37], and behaves as a linear dependence on q as a consequence of the collective excitation mode of the surface-localized states. The intrinsic acoustic mode at zero temperature is exclusive for multilayer graphene systems with the specific ABC stacking configuration. The linear plasmon dispersion, well defined up to 0.25 eV, is describable by the band-structure effect. Distinct from the $\sqrt{q}$ dispersion of the 2D electron gas and from that of the monolayer graphene, such a plasmon mode displays strong damping and disappears at small $q \simeq 0.01$ Å^{-1} (the SPE boundary of $S_1^v \to S_2^c$ and $S_1^v \to S_3^c$). After this region, the optical plasmon $\omega_p^{2\text{nd}}$ is formed near $\omega \simeq 0.32$ eV, with the plasmon dispersion similar to the $\omega_p^{1\text{st}}$ one. These two modes have a similar dispersion which is mainly attributed to the same $S_1^v \to S_1^c$ interband excitation channel. Another prominent characteristic of the $\omega_p^{2\text{nd}}$ mode is that its frequency reaches up to 0.6 eV. This can be manifested by fact that the high DOS of the $S_1^{c,v}$ subbands prevents the coupling from other interband excitations.

The plasmon modes are improved by doping to increase the free charge density in the extrinsic condition. As E_F is increased, the interband and intraband excitations lead to new plasmon modes and diversified phase diagrams. Plasmons with different dispersion relationships are revealed at $E_F = 0.1$ eV, as shown in Figs. 3(b) and 3(c). They behave as acoustic and optical modes in the low and middle (q, ω) regions enclosed

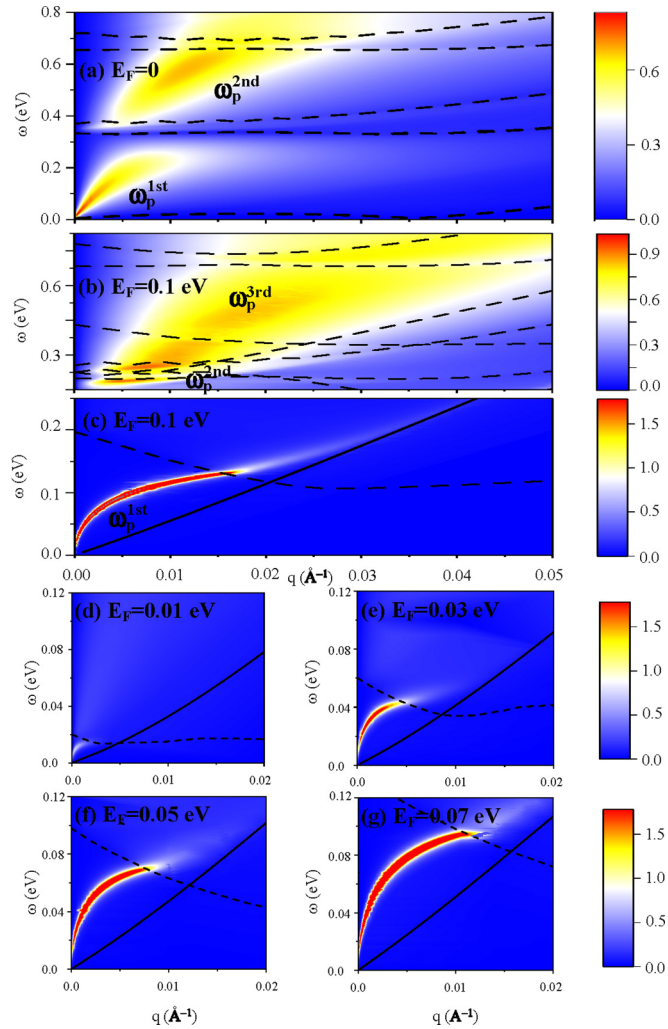

FIG. 3. (a)–(c) (q, ω)-excitation phase diagram of ABC-stacked trilayer graphene for $E_F = 0$ and 0.1 eV. (d)–(g) Low-energy plasmons for $E_F = 0.01$, 0.03, 0.05, and 0.07 eV. The boundaries of SPE channels are shown by solid and dashed curves, indicating the onset and end energies of the intraband and interband transitions.

by the SPE boundaries. The acoustic mode is prominent in the region without SPEs, while showing strong damping when dispersing into the region of the $S_1^v \to S_1^c$ interband SPEs. Its intensity quickly drops by more than one order of magnitude at $q \simeq 0.017$ Å^{-1} and disappears beyond $q \simeq 0.05$ Å^{-1}, a characteristic being dominated by the nearest vertical interlayer atomic interaction γ_1. On the other hand, the optical mode is separated into several parts, each of which appears with different degrees of Landau damping in a specified domain. For $0.3\,\text{eV} \leqslant \omega \leqslant 0.4\,\text{eV}$, the plasmon dispersion is approximately flat, reflecting the particular partially flat subbands. In addition to the original interband channels, the induced free carriers also contribute to the optical plasmon.

The acoustic plasmon deserves a closer examination in the low-energy region. With an increment of E_F, the collective excitation channel is transformed from an interband $(S_1^v \to S_1^c)$ to intraband $(S_1^c \to S_1^c)$. Accordingly, the acoustic plasmon deviates from the linear dispersion of the pristine graphene even in the case of weak doping, in Figs. 3(d)–3(g). The

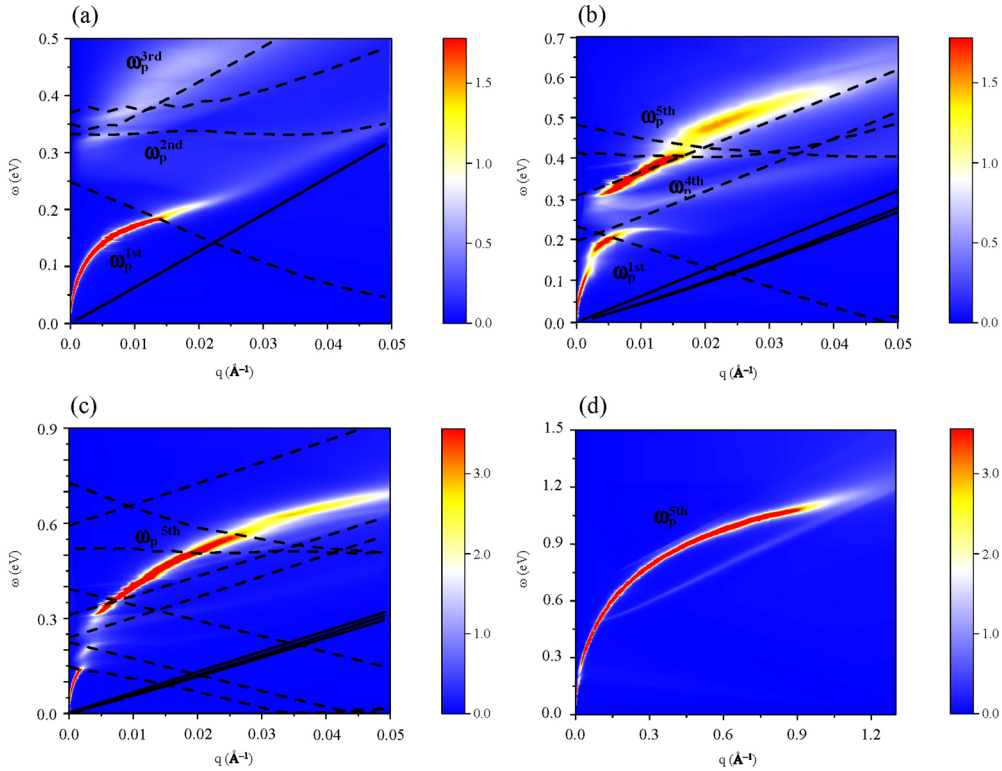

FIG. 4. (q, ω)-excitation phase diagrams of ABC-stacked trilayer graphene at (a) $E_F = 0.3$ eV, (b) $E_F = 0.4$ eV, (c) $E_F = 0.5$ eV, and (d) $E_F = 0.8$ eV.

dispersion and intensity of the acoustic plasmon are enhanced, because the intraband collective excitations gradually become predominant in the plasmon spectra. Furthermore, the acoustic mode extends over a wider (q, ω) range than in the case of zero doping as the SPE boundaries shift to higher q and ω. The existence of the acoustic plasmons with different dispersion relationships indicates the effects of the band structure and the doping carrier densities.

With a variation of E_F, phase diagrams are dramatically changed due to the conservation of the transferred momentum q and the energy ω, as shown in Fig. 4. At $E_F = 0.3$ eV [Fig. 4(a)], the plasmon modes extend to a higher energy due to the increasing free carriers. The most striking behavior of the ω_p^{1st} acoustic mode is its enhanced intensity and square-root dispersion, which are in sharp contrast to the acoustic plasmon in cases of zero and low dopings. Nevertheless, if the subbands S_2^c and S_3^c are partially occupied, the plasmon modes are drastically changed. At $E_F = 0.4$ eV [Fig. 4(b)], the acoustic plasmon arises from the three kinds of intraband excitations, i.e., $S_i^c \to S_i^c$ $(i = 1, 2, \text{and } 3)$. In addition, the interplay between interband and intraband excitations also gives rise to new plasmon modes and diversified phase diagrams. According to the band effects, the Landau damping is strong for the induced interband SPEs, e.g., $S_1^c \to S_2^c$ and $S_1^c \to S_3^c$. In the region of $0.2 \text{ eV} \leqslant \omega \leqslant 0.3$ eV, the ω_p^{4th} plasmon mode has a concave upward dispersion; it has an onset energy of negative dispersion about 0.3 eV and disperses upward for $q \gtrsim 0.01$ Å^{-1}. The weak plasmon intensity indicates robust Landau dampings associated with the particular partially flat and sombrero subbands. On the other hand, the ω_p^{5th} mode is enhanced and shifted to higher ω by the induced collective excitation channels. With a further increase of E_F, the plasmon is hardly affected by the Landau dampings associated with the induced interband SPEs. At $E_F = 0.5$ eV [Fig. 4(c)], the various plasmons gradually merge into a long-range acoustic mode, ω_p^{5th}, because the collective excitations from the free carriers dominate the electronic excitations. Under a heavy doping condition, e.g., $E_F = 0.8$ eV [Fig. 4(d)], there exists only one strong acoustic mode, ω_p^{5th}, over a wide region in the (q, ω)-excitation phase diagram.

Trilayer ABC-staked graphene is predicted to exhibit rich and unique Coulomb excitations. There are a lot of SPE channels and five kinds of plasmon modes, mainly arising from three pairs of energy bands and doping carrier densities. Their complicated relations create the diverse (q, ω)-excitation phase diagrams. The plasmon peaks in the energy-loss spectra might decline and even disappear under various Landau dampings. The linear acoustic plasmon is related to the surface states in pristine systems, while it becomes a square-root acoustic mode at any doping. Specifically, all the layer-dependent atomic interactions and Coulomb interactions have been included in the polarization function and dielectric function. The theoretical framework of the layer-based RPA could be further generalized to study the e-e interactions in emergent 2D materials, e.g., silicene [38] and right germanene [8].

This work was supported in part by the Ministry of Science and Technology of Taiwan, the Republic of China, under Grant No. NSC 105-2112-M-006 -002 -MY3.

[1] K. S. Novoselov, A. K. Geim, S. V. Morozov, D. Jiang, Y. Zhang, S. V. Dubonos, I. V. Grigorieva, and A. A. Firsov, Science **306**, 666 (2004).

[2] X. Dou, A. Jaefari, Y. Barlas, and B. Uchoa, Phys. Rev. B **90**, 161411(R) (2014).

[3] A. H. Castro Neto, F. Guinea, N. M. R. Peres, K. S. Novoselov, and A. K. Geim, Rev. Mod. Phys. **81**, 109 (2009).

[4] J. Y. Wu, S. C. Chen, O. Roslyak, G. Gumbs, and M. F. Lin, ACS Nano **5**, 1026 (2011).

[5] T. Stauber and H. Kohler, Nano Lett. **16**, 6844 (2016).

[6] R. Roldan and L. Brey, Phys. Rev. B **88**, 115420 (2013).

[7] J. H. Ho, C. L. Lu, C. C. Hwang, C. P. Chang, and M. F. Lin, Phys. Rev. B **74**, 085406 (2006).

[8] P. H. Shih, C. W. Chiu, J. Y. Wu, T. N. Do, and M. F. Lin, Phys. Rev. B **97**, 195302 (2018).

[9] S. J. Park and R. E. Palmer, Phys. Rev. Lett. **105**, 016801 (2010).

[10] F. J. Nelson, J.-C. Idrobo, J. D. Fite, Z. L. Mišković, S. J. Pennycook, S. T. Pantelides, J. U. Lee, and A. C. Diebold, Nano Lett. **14**, 3827 (2014).

[11] A. Politano, I. Radović, D. Borka, Z. L. Mišković, H. K. Yu, D. Farías, and G. Chiarello, Carbon **114**, 70 (2017).

[12] P. Wachsmuth, R. Hambach, M. K. Kinyanjui, M. Guzzo, G. Benner, and U. Kaiser, Phys. Rev. B **88**, 075433 (2013).

[13] C. F. Chen, C. H. Park, B. W. Boudouris, J. Horng, B. Geng, C. Girit, A. Zettl, M. F. Crommie, R. A. Segalman, S. G. Louie, and F. Wang, Nature (London) **471**, 617 (2011).

[14] C. Kramberger, E. Einarsson, S. Huotari, T. Thurakitseree, S. Maruyama, M. Knupfer, and T. Pichler, Phys. Rev. B **81**, 205410 (2010).

[15] C. Y. Lin, J. Y. Wu, Y. J. Ou, Y. H. Chiu, and M. F. Lin, Phys. Chem. Chem. Phys. **17**, 26008 (2015).

[16] M. Koshino and E. McCann, Phys. Rev. B **80**, 165409 (2009).

[17] C. Y. Lin, T. N. Do, Y. K. Huang, and M. F. Lin, *Optical Properties of Graphene in Magnetic and Electric Fields* (IOP Publishing, Bristol, UK, 2017).

[18] Z. Jiang, E. A. Henriksen, L. C. Tung, Y. J. Wang, M. E. Schwartz, M. Y. Han, P. Kim, and H. L. Stormer, Phys. Rev. Lett. **98**, 197403 (2007).

[19] K. S. Novoselov, A. K. Geim, S. V. Morozov, D. Jiang, M. I. Katsnelson, I. V. Grigorieva, S. V. Dubonos, and A. A. Firsov, Nature (London) **438**, 197 (2005).

[20] H. G. Yan, X. S. Li, B. Chandra, G. Tulevski, Y. Q. Wu, M. Freitag, W. J. Zhu, P. Avouris, and F. N. Xia, Nat. Nanotechnol. **7**, 330 (2012).

[21] H. G. Yan, T. Low, W. J. Zhu, Y. Q. Wu, M. Freitag, X. S. Li, F. Guinea, P. Avouris, and F. N. Xia, Nat. Photonics **7**, 394 (2013).

[22] T. Low and P. Avouris, ACS Nano **8**, 1086 (2014).

[23] Y. C. Fan, N. H. Shen, T. Koschny, and C. M. Soukoulis, ACS Photonics **2**, 151 (2015).

[24] Y. C. Fan, N. H. Shen, F. L. Zhang, Q. Zhao, Z. Y. Wei, P. Zhang, J. J. Dong, Q. H. Fu, H. Q. Li, and C. M. Soukoulis, ACS Photonics **5**, 1612 (2018).

[25] R. Xu, L. J. Yin, J. B. Qiao, K. K. Bai, J. C. Nie, and L. He, Phys. Rev. B **91**, 035410 (2015).

[26] D. Pierucci, H. Sediri, M. Hajlaoui, J. C. Girard, T. Brumme, M. Calandra, E. Velez-Fort, G. Patriarche, M. G. Silly, G. Ferro, V. Souliere, M. Marangolo, F. Sirotti, F. Mauri, and A. Ouerghi, ACS Nano **9**, 5432 (2015).

[27] Y. Que, W. Xiao, H. Chen, D. Wang, S. Du, and H.-J. Gao, Appl. Phys. Lett. **107**, 263101 (2015).

[28] K. F. Mak, J. Shan, and T. F. Heinz, Phys. Rev. Lett. **104**, 176404 (2010).

[29] L. B. Biedermann, M. L. Bolen, M. A. Capano, D. Zemlyanov, and R. G. Reifenberger, Phys. Rev. B **79**, 125411 (2009).

[30] J. Borysiuk, J. Sołtys, and J. Piechota, J. Appl. Phys. **109**, 093523 (2011).

[31] N. T. T. Tran, S. Y. Lin, C. Y. Lin, and M. F. Lin, *Geometric and Electronic Properties of Graphene-Related Systems: Chemical Bondings* (CRC Press, Boca Raton, FL, 2017).

[32] P. R. Wallace, Phys. Rev. **71**, 622 (1947).

[33] J.-C. Charlier, J.-P. Michenaud, and Ph. Lambin, Phys. Rev. B **46**, 4540 (1992).

[34] C. Coletti, S. Forti, A. Principi, K. V. Emtsev, A. A. Zakharov, K. M. Daniels, B. K. Daas, M. V. S. Chandrashekhar, T. Ouisse, D. Chaussende, A. H. MacDonald, M. Polini, and U. Starke, Phys. Rev. B **88**, 155439 (2013).

[35] R. Egerton, *Electron Energy-Loss Spectroscopy in the Electron Microscope*, 3rd ed. (Springer, Berlin, 2011).

[36] A. Kawabata and R. Kubo, J. Phys. Soc. Jpn. **21**, 1765 (1966).

[37] P. Nozières and D. Pines, Phys. Rev. **109**, 1062 (1958).

[38] J. Y. Wu, S. C. Chen, G. Gumbs, and M. F. Lin, Phys. Rev. B **94**, 205427 (2016).